Materials Advances

ROYAL SOCIETY OF CHEMISTRY

PAPER

View Article Online
View Journal | View Issue

Cite this: *Mater. Adv.*, 2024, 5, 7659

Enhanced efficiency of dye-sensitized solar cells *via* controlled thickness of the WO_3 Langmuir–Blodgett blocking layer in the Debye length regime†

Neeraj Kumar,[ad] Sipra Choudhury,[bd] Aman Mahajan[c] and Vibha Saxena*[ad]

Received 22nd January 2024,
Accepted 21st August 2024

DOI: 10.1039/d4ma00063c

rsc.li/materials-advances

Generally, a thin (>50 nm) transition metal oxide (TMO) film (such as TiO_2) is employed as an interfacial layer (also called a blocking layer, BL) between FTO and mesoporous TiO_2 in a dye-sensitized solar cell (DSC). The function of this layer is to provide full coverage of FTO so as to reduce back electron recombination without compromising transparency and charge transport properties. Recent research has demonstrated that WO_3 has better charge transport and stability than TiO_2 and therefore has the potential to be employed as a hole blocking layer. Furthermore, ultra-thin TMO films having thickness less than the Debye length (characteristic length of the space charge layer in the WO_3, L_D) are expected to provide better interfacial and optical properties. However, reducing the thickness in such thin films has been challenging owing to available preparation methods. In this work, the Langmuir–Blodgett (LB) technique has been adopted to prepare high quality crystalline BL of WO_3 of controlled thickness in the range of L_D (4–20 nm). The interfacial properties such as charge transport and blocking behaviour of WO_3 LB films improved significantly when the thickness was reduced to ≤14 nm, which is comparable to L_D. As a result, DSCs fabricated with thinner WO_3 BL (thickness ≤14 nm) showed significant efficiency (η) improvement (22%) leading to η up to 9.79% *vis à vis* DSCs with WO_3 BL having thickness 20 nm.

1. Introduction

In the last decade, dye sensitized solar cells (DSCs) have emerged as potential alternatives to Si solar cell technology on account of their various advantages, such as flexibility, low cost, simple fabrication techniques, lightweight and efficient working even under diffused light.[1,2] The key challenges in developing highly efficient DSCs have been to simultaneously improve the light-harvesting of the active layer and to reduce the recombination losses at various interfaces. Conventionally, a thin transition metal oxide (TMO) film, such as TiO_2 (>50 nm), is employed as an interfacial layer between the FTO substrate and mesoporous TiO_2 (m-TiO_2) layer (blocking layer, BL) in DSCs, which prevents undesired recombination of photon-generated electrons. This BL also helps in tuning the work function and providing better interfacial properties to enable efficient electron transport.[3–5] In addition to TiO_2, other metal oxide films such as SnO_2, Fe_2O_3, ZnO and Nb_2O_5 have also been employed as BL in DSCs in order to enhance efficiency.[6]

WO_3 has been used extensively for a variety of applications, such as smart windows,[7] photocatalysts and gas sensors, because of its excellent chemical stability, high work function (~6.2 eV) and carrier mobility (5–12 $cm^2\ V\ s^{-1}$), and tunability of electronic structures through the polymorph.[8–11] However, WO_3 films in solar cells have not been used much as interfacial layers due to low conductivity, amorphous structure, mediocre interfacial charge transfer and unfavorable conduction band (CB) position.[12,13] Therefore, it is essential to achieve high crystallinity, uniformity, and transparency with suitable work function in WO_3 films so that it can provide preferential percolation paths for the charge transport without compromising optical transmittance.[14,15] Furthermore, it has been reported in the literature that reducing the thickness of a uniform TMO film to the Debye length (characteristic length of the space charge layer in the TMO, L_D) will yield higher electrical conductivity without compromising optical transmittance.[16] The L_D is dependent on the dielectric constant (ε) and carrier density (N_D) as follows:

$$L_D = \sqrt{\frac{\varepsilon k T}{q^2 N_D}} \quad (1)$$

[a] *Technical Physics Division, Bhabha Atomic Research Centre, Trombay, Mumbai 40085, India. E-mail: vibhas@barc.gov.in*
[b] *Chemistry Division, Bhabha Atomic Research Centre, Trombay, Mumbai 40085, India*
[c] *Department of Physics, Guru Nanak Dev University, Amritsar 143005, India*
[d] *Homi Bhabha National Institute, Mumbai 40094, India*

† Electronic supplementary information (ESI) available. See DOI: https://doi.org/10.1039/d4ma00063c

where k, T and q are the Boltzmann constant, temperature and unit charge, respectively.

The L_D of the WO_3 is reported to be in the range of 2–20 nm and therefore, it is anticipated that WO_3 films having thickness in this range (<20 nm) could lead to charge transport behavior different from what is observed for thicker films (>20 nm).[17] Moreover, for TMO having thicknesses $\leq L_D$, the space charge layer (SCL) can extend beyond the film thickness. This will eventually lead to different charge distributions near the film–substrate interface and hence, influence the interfacial properties such as charge transport and blocking behavior. Even though reducing the BL thickness is known to be effective for improving the interfacial properties without loss of optical transmittance, preparing such an ultra-thin (<20 nm) uniform film is challenging.

Amongst available techniques to deposit ultra-thin films, sputtering, pulsed layer deposition (PLD), atomic layer deposition (ALD) and molecular beam epitaxy (MBE) have been used widely[18–22] for depositing WO_3 films. The films, prepared by thermal evaporation, resulted in amorphous structure and rough morphology. Post annealing (>300 °C) employed to induce crystallization, however, led to shrinkage of the material, forming wide cracks owing to the increase in overall residual stresses in the film.[23] Spark ablation was also used to prepare ultra-thin WO_3 films, and enhanced NO_2 gas sensing was reported.[24] However, the films had many cracks in as-deposited as well as annealed films. Mattoni *et al.* reported crystalline ultra-thin WO_3 (9 nm) on top of TiO_2-terminated $SrTiO_3$(001) substrates using the PLD technique.[25] The film decorated with Pt resulted in increased sub-ppm hydrogen sensing owing to the crystalline structure and high surface area–volume ratio.[26] Ultra-thin WO_3 films were also produced using ALD from different precursors such as WF_6, *in situ*-generated hexavalent tungsten oxyfluoride, $(t\mathrm{BuN})_2(\mathrm{NMe}_2)_2\mathrm{W}$, and hexacarbonyl precursor $W(CO)_6$.[27] However, low growth per cycle (<0.2 Å), high impurity incorporation, and non-stoichiometric composition limited their use for device applications. Furthermore, a plasma-enhanced ALD process was reported, however, a polycrystalline film of monoclinic phase could be obtained only at elevated temperature ~ 400 °C.[28] Though ALD has the advantages of atomic level conformal coverage of a high quality and crystalline film on the substrate, high material cost and consumption as well as high wastage limits the industrial applicability of this technique. Therefore, present techniques for depositing ultra-thin WO_3 films have the following disadvantages: (i) limited control over the quality of deposited films of different thicknesses, (ii) the necessity of specific substrates, corrosive precursor or co-reactants, (iii) the requirement of high vacuum and high deposition temperature and (iv) non-scalability. Therefore, the reported literature on BL materials in solar cells has mainly been focused on materials which could provide full coverage of the FTO substrate without loss of optical transmittance. It is to be emphasized here that the effect of BL thickness on the DSC performance has not been studied extensively for film thicknesses <20 nm due to the limitation of uniform film coverage by most of the reported preparation techniques[6,18,19] and therefore, there is a lot of room for developing alternative materials for enhancing device efficiency through maximizing intrinsic BL properties.

In this context, the Langmuir–Blodgett (LB) technique is a very simple, environment-friendly, and versatile method for preparing ordered multilayers of a wide range of materials, such as carbon nanomaterials, conductive polymers, *etc.* with low consumption of materials. In addition, this technique allows control over the morphology, thickness and molecular architecture of films through suitable manipulation of the subphase pH, barrier speed, deposition speed, and post-transfer treatments along with the possibility of low temperature processing. In the present work, crystalline ultra-thin (4–20 nm) WO_3 films were prepared from the thermal decomposition of the WO_3-octadecyl amine (ODA) complex ($WO_{3,ODA}$) of multilayers, using the LB technique. The interfacial properties of the prepared films were thoroughly characterized using UV-Vis spectroscopy, electrochemical techniques, ellipsometry, Kelvin-probe and field-emission scanning electron microscopy (FESEM). A significant improvement in blocking and charge transport behavior is observed for films thinner than ≤ 14 nm (within L_D regime) as compared with thick 20 nm WO_3 films (beyond the L_D regime). The films, when employed in the fabrication of DSCs, show significant improvement in efficiency (η) up to 9.79% as compared to those with thicker ($>L_D$) WO_3 BL films ($\eta \sim 8.02\%$). The electrochemical impedance spectroscopy (EIS) and intensity-modulated photocurrent/photovoltage spectroscopy (IMVS/IMPS) data suggested improved charge transport and reduced recombination in DSCs with thinner ($\leq L_D$) WO_3 BL as compared with those with thick BL ($>L_D$).

2. Experimental section

Chloroform and other chemicals were of analytical grade or higher purity and were used without any further purification. Deionized (DI) water (Milli-Q, Millipore) having resistance 18 MΩ was used to prepare solutions. The preparation of LB multilayers of $WO_{3,ODA}$ was carried out using a KSV-Nima Langmuir trough equipped with two Teflon barriers with a total area of 850 cm^2. The absence of surface-active contaminants was verified by compressing the subphase to achieve surface pressure ≤ 0.1 mN m^{-1}. Then, 50 μL of octadecyl amine solution in chloroform (1 mg mL^{-1}) was spread on the subphase containing 0.15 mM sodium tungstate solution (pH $\sim$ 7) in DI water, using a Hamilton micro-syringe. After 20 mins to evaporate solvent, the layer was simultaneously compressed by two compression barriers at the rate of 5 mN m^{-1} min^{-1}. The FTO substrates were cleaned by successive sonication in warm Hellmnax soap, DI water, acetone, methanol, and isopropyl alcohol and then dried with nitrogen gas, whereas Si substrates were cleaned using a Piranha solution. All substrates were further cleaned by using atmospheric plasma (Harrick Plasma, model PDC-002) in ambient air for 10 min before carrying out multilayer deposition. Multilayers were transferred in successive downstrokes and upstrokes with a 10 min interval between the upstroke and the subsequent downstroke. The dipping rate

was 5 mm min^{-1} in both directions. The transfer of the LB multilayers was Y type and the transfer ratio was 90–100% onto FTO and Si substrates. The films were subsequently thermally decomposed at 400 °C for 5 h. In order to compare the results, WO_3 films were also prepared by spin casting, using a neutral surfactant-(polyethylene glycol) assisted tungsten precursor as reported earlier.[29] The thickness of the prepared films on Si substrates was estimated using variable angle spectroscopic ellipsometry (Sentech SE400adv) at wavelength 632 nm. For device fabrication, a slightly modified procedure of preparing photoanode in our earlier work was adopted.[30] The photoanode was prepared by doctor blading mesoporous TiO_2 paste (Solaronix, Ti-nanoxide T/SP) and a scattering layer of TiO_2 paste (Solaronix, Ti-nanoxide R/SP) on the plasma treated WO_3 BL/FTO substrate. The films were sintered at 500 °C using a multi-step temperature program. This was followed by a post-treatment with 40 mM $TiCl_4$ aqueous solution at 70 °C for $\frac{1}{2}$ h and subsequently annealing at 500 °C for $\frac{1}{2}$ h. The photoanodes were sensitized using a solution of 0.5 mM N719 dye (Solaronix) with 5 mM cholic acid in *tert*-butyl alcohol/acetonitrile (1 : 1 v/v). The devices (area 0.12 cm^2) were fabricated using a pre-drilled platinum coated counter electrode. The electrochemical as well as photovoltaic characterization was performed using a Potentiostat/Galvanostat (PGSTAT 30, Autolab Eco Chemie, Netherlands). The surface morphology was analyzed using a FESEM (Carl Zeiss Supra 55, SEM micrograph) as well as atomic force microscopy (AFM) (Anton Paar Tosca TM 400) in tapping mode. UV-Vis spectroscopy was carried out using a double beam UV-Vis spectrophotometer (Jasco, V 530). The Fourier transform infrared spectroscopy (FTIR) of LB films deposited on Si substrates was carried out, in reflectance mode, using a Bruker spectrometer (model: Vertex 80 V) at a resolution of 4 cm^{-1}. X-ray photoelectron spectroscopy (XPS) data measurements were carried out using the RIBER MBE system, which was equipped with a Mg K_α source. The binding energy scale was calibrated to the Au $4f_{7/2}$ line of 83.95 eV. Raman spectra of LB films, deposited on Si substrates, were recorded on a Jobin-Yvon micro-Raman spectrometer (LabRAM HR800), in the 180° backscattering geometry, with a spectral resolution of 1 cm^{-1} using a HeNe Laser. The laser beam was focused onto the sample using a ×100 objective lens and the laser spot size was ~5 μm. Kelvin probe scanning microscopy (model: KP Technology), having resolution of ~0.003 eV, was employed to measure the work function of spin cast and LB WO_3 films on FTO substrates. Electrochemical characterizations of all BLs were carried out using a one-compartment, three-electrode electrochemical cell: FTO or FTO/WO_3 performed as the working electrode, while Ag/AgCl and platinum electrodes were used as reference and counter electrodes, respectively. The EIS measurements were done in a range from 100 mHz to 500 kHz by applying an AC voltage of 10 mV superimposed on a dc voltage. For dark EIS measurements, data were collected at dc bias of open-circuit voltage (V_{OC}), V_{OC} ± 0.02 V and V_{OC} ± 0.04 V. The results were analyzed using an equivalent circuit model fitted with ZSimpWin 3.22 software. IMPS/IMVS measurements were carried out under a Green LED (wavelength 530 nm), which provided the DC illumination bias, superimposed with AC modulation ~10% of the DC intensity. The measurements were performed between 1 kHz and 100 mHz, 20 data points per decade. The current–voltage (*J*–*V*) characteristics of the DSCs were recorded under 1 sun simulated AM 1.5G illumination using a solar simulator (G2V, Canada). The intensity of the source was calibrated using a reference silicon cell before recording the characteristics.

3. Results and discussion

3.1 Surface properties of the $WO_{3,ODA}$ monolayer and structure of $WO_{3,ODA}$ Langmuir–Blodgett multilayers

Since the lateral organization of the ODA molecules on the subphase may influence the $WO_{3,ODA}$ monolayer formation and subsequent multilayer deposition, the surface properties of monolayer organization and packing were investigated by recording surface pressure–mean molecular area (π–*A*) isotherms and are presented in Fig. 1(a). At large area, *i.e.* at the start of barrier compression, (zero surface pressure) a gas phase at the air–water interface is observed. The presence of WO_4^{2-} ions in the subphase results in an increased expansion of the

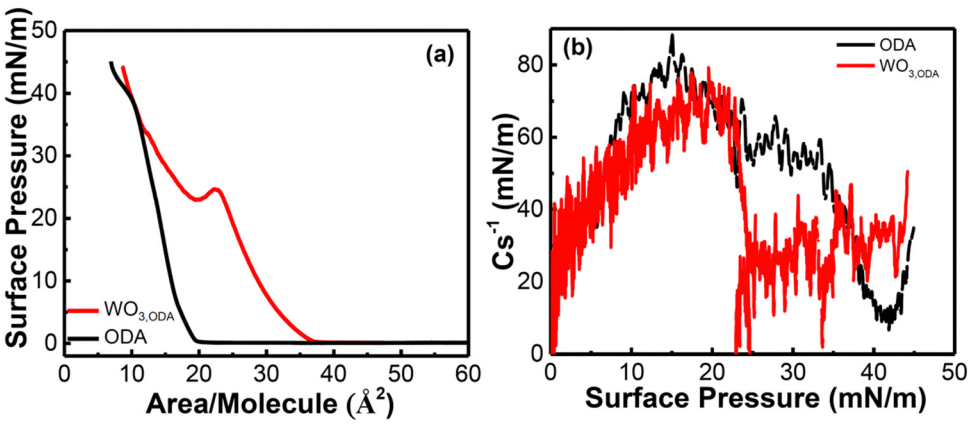

Fig. 1 (a) Surface pressure isotherm and (b) compressibility of ODA and $WO_{3,ODA}$ monolayers.

ODA monolayer as evident by an increase in the lift-off area (36.8 Å^2) of the ODA monolayer spread on tungstate salt subphase. Distinct transition phases can be observed in the presence of WO_4^{2-} ions in the subphase, which indicates an interaction between WO_4^{2-} ions and ODA. This interaction occurs because the ODA molecules undergo protonation in the presence of water resulting in positive head groups ($R\text{-}NH_3^+$). This positive charge interacts with anionic WO_4^{2-}, resulting in an electrostatic interaction between the two groups. In the range 10–20 mN m^{-1}, it is more clearly discerned in the presence of WO_4^{2-} ions than in pure water isotherms where transition phases occur suddenly because of fast condensation of the ODA molecules. Moreover, an additional slope change takes place around 25 mN m^{-1}, where a kink is observed. When ODA is compressed beyond this, a steep slope of the π–A curve is observed, indicating a phase transition. This is different for the isotherm of the ODA monolayer, for which the lift off area $\sim$21 Å^2 per molecule is estimated, consistent with the reported values found in the literature.[31] Transition phases are not observed in this isotherm, suggesting that a direct transition from a gas to a condensed phase takes place. In order to further elucidate phase transitions and to characterize the interactions of WO_4^{2-} ions with the ODA monolayer, as well as to examine changes in the interfacial packing properties, two-dimensional compressibility of the Langmuir monolayers was investigated. The compressibility coefficient was calculated as per the following equation:

$$C_s^{-1} = A\frac{d\pi}{dA} \quad (2)$$

while C_s^{-1} is low in the gas phase, it increases at the liquid-expanded (LE) and liquid-condensed (LC) phases due to difficulty in deforming the monolayer. The maximum values of the C_s^{-1} provide information on the monolayer phase: the values in the range of 100–250 mN have been associated with the LC phase, and solid phase.[32] Fig. 1(b) shows the isothermal compressibility of the $WO_{3,ODA}$ as well as ODA monolayer at the air–water interface. As shown in the figure, for both cases, the C_s^{-1} value increases as the molecules reorganize to a more condensed state. After the maximum, the condensed state is completed and the C_s^{-1} decreases. For ODA on pure water, a steady increase of the surface pressure starting from 0 to 15 mN m^{-1} was observed, and after 15 mN m^{-1}, the modulus decreases. The C_s^{-1}–π curve for ODA monolayers on subphase containing WO_3 salt is entirely different from that of ODA monolayers on pure water. Two peaks can be distinguished in the figure at 15–20 mN m^{-1} and 38–40 mN m^{-1}, clearly suggesting a phase transition. Lower values of C_s^{-1} were obtained for $WO_{3,ODA}$ as compared to that of ODA monolayers suggest low rigidity and compaction of the $WO_{3,ODA}$ monolayer. The difference in C_s^{-1}–π curves in the LC region confirms molecular interactions of WO_4^{2-} anions with ODA molecules. Since the $WO_{3,ODA}$ monolayer is the building block of the WO_3 films and close packed at the maximum point in the C_s^{-1}–π curve, we chose surface pressure corresponding to this lowest C_s ($\sim$15 mN m^{-1}) to deposit multilayers. For this purpose, $WO_{3,ODA}$ monolayers were transferred to the substrate at constant pressure multiple times and were subsequently decomposed thermally. The phase/structure of the multilayered films after thermal decomposition was investigated using FTIR, XPS, and Raman spectroscopy (Fig. 2). As shown in Fig. 2(a), the FTIR spectra of the thermally decomposed film showed significant reduction of the C–H stretching vibration bands of the hydrocarbon chains at 2919 cm^{-1} (asymmetric) and 2851 cm^{-1} (symmetric) and complete removal of the C–H bending mode, at 1470 cm^{-1}, of the CH_2 group. It is to be noted that these peaks were clearly observed in the $WO_{3,ODA}$ films. This confirms that the hydrocarbon part in $WO_{3,ODA}$ is removed after thermal decomposition. The stoichiometric WO_3 phase was confirmed by X-ray photoelectron spectroscopy (Fig. 2(b), which when deconvoluted, show peaks corresponding W $4f_{5/2}$ and $4f_{7/2}$ doublet peaks at 37.9 eV and 35.8 eV, respectively (W^{6+} state) and in accordance with the reported literature values for WO_3.[33] It should be noted that the de-convoluted core level spectrum for the spin cast WO_3 film showed (i) a shifting of 0.7 eV towards higher binding energy for doublet peaks, *i.e.* the appearance of W $4f_{5/2}$ and W $4f_{7/2}$ peaks at 38.6 eV and 36.5 eV, respectively and (ii) two smaller contributions from the second doublet at lower binding energy, (W $4f_{5/2}$ = 37.9 eV and W $4f_{7/2}$) = 35.8 eV, in addition to peaks for W $4f_{7/2}$ and W $4f_{5/2}$ states. This suggests sub-stoichiometry and the existence of defects due to the presence of W^{5+} states in the spin cast film.[33] A shift in doublet, observed in spin cast films, towards higher binding energy as relative to stoichiometric WO_3 has been attributable to the presence of a large degree of oxygen deficiency and thereby

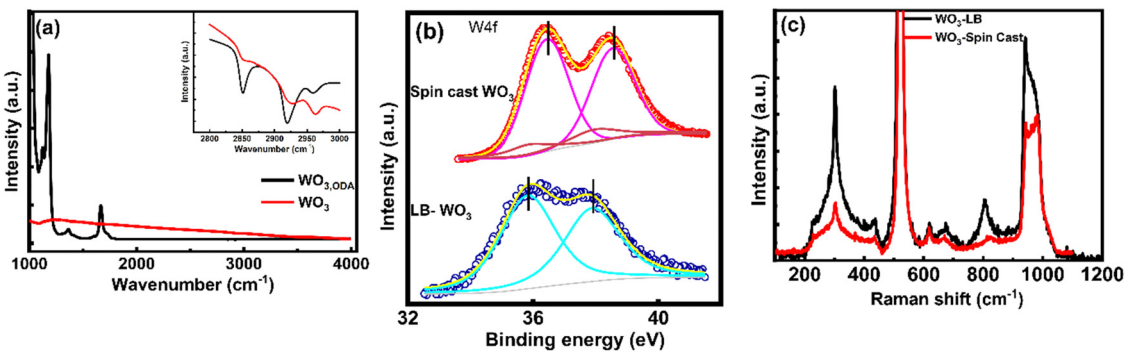

Fig. 2 (a) FTIR of the WO_3 LB film after thermal decomposition, (b) XPS and (c) Raman spectra of the spin cast and WO_3 LB film.

lattice disorder in hydrogen-treated WO_3 films. Large amounts of lattice disorder result in occupation of large density of states within the energy gap with a corresponding shift of the Fermi level toward higher energies. Other than stoichiometry, spin cast and LB WO_3 films also differ in their crystallinity as depicted in Raman data (Fig. 2(c)). The features at 303, 435, 622, and 675 cm^{-1} show the presence of Si–O bonds due to the substrate.[34] A well-defined peak at $\sim$810 cm^{-1} is observed for WO_3 LB films confirming the formation of the tetragonal phase of WO_3 as observed earlier for ultra-thin films. Two major features are observed in the case of the spin cast WO_3 film: the peak at 810 cm^{-1} is (i) red-shifted to 826 cm^{-1} owing to the bulk-nature of the spin cast films and (ii) significantly weakened in intensity due to reduced crystallinity.[35] This is consistent with XPS data, which shows increased defect states corresponding to the sub-stoichiometric phase in the spin cast WO_3 films.

3.2 Optical, morphology and blocking properties of ultra-thin WO_3 films

After establishing the fact that thermal decomposition of the $WO_{3,ODA}$ multilayered films yields a stoichiometric and crystalline WO_3 structure, we prepared WO_3 films of various thicknesses by controlling the deposition cycle of $WO_{3,ODA}$ monolayers on the substrate. Different numbers of monolayers, 9, 19, 25, 35 and 50 layers, were deposited and hereafter will be referred to as 9 L, 19 L, 25 L, 35 L and 50 L, respectively. The optical, morphology and interfacial properties of the prepared WO_3 film were studied before employing them as BLs in DSC fabrication and the results are presented as follows:

Since the optical transmittance is strongly affected by dielectric constants, we estimated thickness and optical constants (refractive index, n and extinction coefficient, k) using ellipsometric measurements and fitted data using the model as reported earlier.[30] The estimated n and k of the as-deposited films were found to be in 1.56 and 0.04, respectively. After thermal decomposition, the refractive index ($\sim$2.8) increases and the absorption coefficient decreases ($\sim$0.006), suggesting conversion of the $WO_{3,ODA}$ LB multilayers to WO_3. The high refractive index of all WO_3 films suggests compact and uniform deposition of the film. The thicknesses of the WO_3 multilayers, transferred on Si substrates, were estimated using estimated n and k values and are presented in Fig. 3(a) as a function of number of layers. The thickness of the as-WO_3 film was found to shrink approximately 1/6th after thermal decomposition. The estimated data reveal that a monolayer of $WO_{3,ODA}$ is $\sim$2.4 nm thick and after thermal decomposition, it reduces to $\sim$0.4 nm. It should be noted that as-deposited films were featureless and transparent up to 19 L, and afterwards a semi-transparent film having a brownish tinge was observed. After thermal decomposition, all WO_3 LB films of thickness $\leq$14 nm show enhanced optical transmittance as presented in Fig. 3(b). This might be due to better matching of the refractive index at the FTO/WO_3/air interface than the FTO/air interface (refractive index for FTO $\sim$ 2.4), which reduces internal reflection and therefore results in enhanced transmittance. Slightly reduced transmittance observed for the 20 nm thick film might be due to increased thickness. Typical fringes observed in the spectra of all WO_3 LB films suggest smooth surface morphology of the prepared films; in contrast, such fringes were absent in the spin cast WO_3 film.

The smooth morphologies of the prepared LB films as compared with that of the spin cast film were also confirmed from recorded FESEM images, as depicted in Fig. 4. The FESEM images of WO_3 films are slightly blurred as compared with FTO (inset of Fig. 4(a)) owing to the ultra-thin nature. As compared to the FESEM image of the spin cast WO_3 film, LB deposited WO_3 films were found to be more uniform, pin-hole free and homogeneous. It should be noted that the thickness variation of the WO_3 film from 4 nm to 20 nm did not result in different surface morphologies. The uniformity in the LB deposited film is also supported by the AFM image, which shows a compact film comprising small crystallites after thermal decomposition of $WO_{3,ODA}$ multilayers (Fig. S1, ESI†). It should be noted that though uniform morphologies for WO_3 crystalline films are observed in the SEM and AFM images, lateral uniformity in cm^2 area has been assessed in the best manner using cyclic voltammetry.[30,36] Therefore, the thickness dependence of the interfacial properties, such as blocking and charge transport behaviour, were studied by analyzing their cyclic voltammogram (CV), EIS and Mott–Schottky (MS) plots as described in

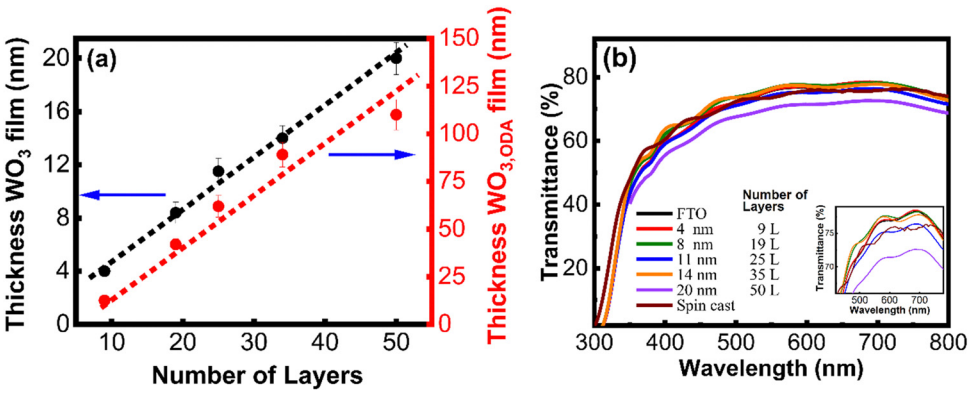

Fig. 3 (a) Estimated thickness and (b) transmittance as a function of number of layers.

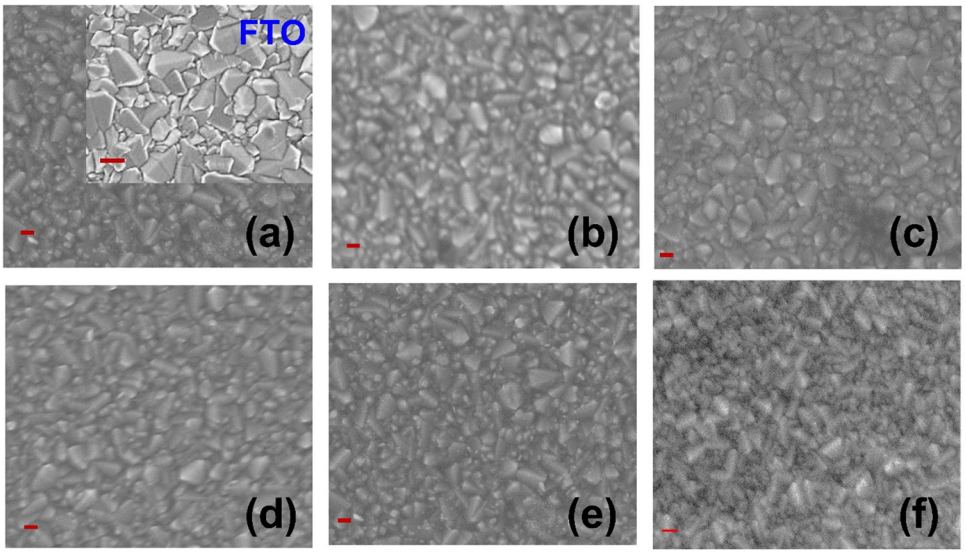

Fig. 4 Top-view FE-SEM images of the prepared WO_3 LB films of thicknesses (a) 4 nm, (b) 8 nm, (c) 11 nm, (d) 14 nm, (e) 20 nm, and (f) the spin cast film, scale bar ~200 nm.

earlier reports[30] (Fig. S2, ESI†). The effectiveness of the blocking effect (BE) of the WO_3 film was estimated by taking into account the percentage suppression of the anodic current in CV as compared to that for the FTO substrate. As shown in Fig. S2(a) (ESI†), all WO_3 LB films showed (i) anodic/cathodic peaks, and (ii) significant suppression of the anodic current as compared to bare FTO and (iii) enhanced cathodic peak, which is due to the electron accumulation below the flat band potential and corresponding reduction of $Fe(CN)_6^{3-}$ at the FTO/WO_3 surface. It is to be noted that $WO_{3,ODA}$ multilayers do not show such features owing to the presence of insulating ODA in the complex. When the film thickness is increased from 4 to 11 nm, good blocking behavior >80% is observed, despite the fact that the thickness of the film is very low (Fig. 5(a)). For 14 nm thick film, the blocking effect is slightly increased and then slightly decreases for 20 nm thick films. The peak-to-peak separation (ΔE) of the anodic and cathodic peaks in the CV follows the trend of blocking effect. This is expected as enhanced thickness of the WO_3 layer poses more and more resistance to charge transfer reaction and therefore the oxidation peak shifts towards positive potential and therefore, results in increased ΔE.

In order to investigate further the thickness effect on blocking behaviour, the EIS spectra of various films were recorded (Fig. S2(b), ESI†). The measured data were fitted using Randle's equivalent circuit model ($R([R_{CT}W]Q)$), where R is the overall contribution of the intrinsic resistance of the WO_3 film, ionic resistance of the electrolyte, and contact resistance comprising connections to the WO_3 electrode, and R_{CT}, Q and W are the charge transfer resistance, constant phase element and Warburg impedance corresponding to WO_3 film, respectively. The capacitance (C_{film}) of the WO_3 film was estimated using estimated Q and R_{CT} values as described earlier[36] and is presented in Fig. 5(b). As shown in the figure, the R_{CT} value increased while the C_{film} decreased with increasing the thickness from 4 nm to 14 nm. These results are indicative of the formation of dense and compact layers. When the film thickness is increased to 20 nm, a slight decrease in charge transfer resistance is observed. The results are consistent with the cyclic voltammetric results where a similar drop in the blocking effect and ΔE has been observed. In order to probe further the thickness dependent interfacial properties of FTO/WO_3, we estimated the capacitance (C_{SC}) of the space charge region, which plays a significant role in the charge distribution at the semiconductor–electrolyte

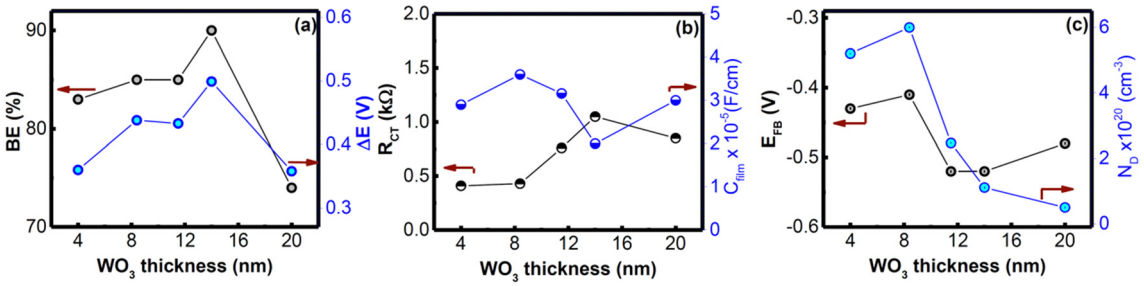

Fig. 5 Estimated (a) blocking effect and ΔE from CV curves, (b) R_{CT} and capacitance across the WO_3 film from EIS spectra and (c) carrier density and flat band potential from the MS plots as a function of WO_3 thickness.

interface. The potential drop in the space charge region, and therefore, the extent of band bending, referred to as ϕ_{SC} (as depicted schematically in ESI,† Fig. S3) is given by the following equation:[37]

$$\phi_{SC} = \frac{kT}{2e}\left(\frac{W}{L_D}\right)^2 \quad (3)$$

where W is the depletion width associated with ϕ_{SC}. The above equation is valid for bulk semiconductors or semiconductors having particle size $\gg L_D$. For nanostructured materials having particle size $\sim L_D$, minimal to no potential drop is present in the space charge region, and band bending can only be obtained for either very highly doped or relatively lower dielectric constant in the material. Neglecting the Helmholtz capacitance, the relationship between the C_{SC} and applied potential is given by the well-known Mott–Schottky equation and has been used to estimate flat band potential (E_{FB}) as well as charge carrier density (N_D) in TMO films.[38,39] For BL thicknesses $\leq$9 nm, the slope of MS curves is similar to that of FTO for WO_3 implying that the space charge region fully extends to the FTO region[40] (Fig. S2c, ESI†). It has been suggested that if the space charge region extends into the FTO substrate, the slope of the MS plot is determined only by dielectric constant and the charge carrier density of the FTO substrate and is not influenced by the film deposited on the substrate.[38] Therefore, estimated N_D and E_{FB} parameters for WO_3 films having thickness $<$11 nm, are not representative of the WO_3 film. Nevertheless, when the film thickness is increased to 11 nm and beyond, a drastic change in slope occurs; therefore, MS plots may be used to determine E_{FB} and N_D values. As shown in Fig. 5(c), the E_{FB} shifts negatively with increasing layer thickness $\geq$11 nm and stabilizes thereafter, suggesting that the dielectric properties of the WO_3 are now dominating the interface properties. Similar kinds of thickness dependent shift in E_{FB} have been observed in the ALD TiO_2 layers and have been attributed to the fact that the (i) crystalline structure starts to be detectable for films thicker than $\sim$15 nm and (ii) for thinner films E_{FB} is largely determined by the FTO substrate.[41] As reported earlier for WO_3 film, the position of CB can be approximated to near E_{FB}[42] and therefore, the change in E_{FB} is correlated with CB position. This means that the conduction band (CB) position of WO_3 is altered depending on the BL thickness in regimes, defined as thick film (20 nm) and thin films ($\leq$11 nm). Subsequently, the interfacial properties, such as the charge transport and recombination, will also differ in both regimes. Furthermore, the decreased charge carrier density for films thicker than 11 nm may be related to the onset of bulk properties of the films as also observed for TiO_2, NiO and SnO_2 films[16,43] and is consistent with CV results, which shows reduced accumulation current for films thicker than 11 nm (Fig. S2, ESI†). A drastic change in the carrier density observed for NiO and SnO_2 films with thickness reduction has been attributed to the space-charge effect as governed by ϕ_{SC}. For carrier density in WO_3 films ranging from 0.5–5 $\times$ 10^{20} cm^{-3}, the calculated L_D is 2–4 nm. Therefore, for film thickness up to 14 nm ($\sim$2–3L_D), the ϕ_{SC} is very small and so negligible band bending occurs at the FTO/WO_3 interface. This leads to an efficient electron transfer across the FTO/WO_3 interface. For films having thickness $\sim$20 nm, which is large compared to the L_D, the films are bulk-like. This gives rise to large ϕ_{SC} and thereby, large band bending at the FTO/WO_3 interface. The presence of a barrier, therefore leads to reduced electron transfer at the FTO/WO_3 interface. This, in turn, enhances the recombination probability at the interface and leads to reduced charge collection at the FTO/WO_3 interface. As a result of sluggish charge transport, thicker films (20 nm) show slightly reduced blocking efficiency than thinner films ($\leq$14 nm).

3.3 Influence of WO_3 BL thickness on photovoltaic properties

The effect of the variation of the thickness of the blocking WO_3 layer on DSCs performance was studied by recording current density (J)–voltage (V) curves under AM 1.5 illumination and in the dark (Fig. 6a and b). All devices showed high efficiency (8% or greater) as compared with the DSC fabricated with spin cast WO_3 BL, which shows low efficiency ($\sim$7%) due to low fill factor (FF) and V_{OC}. The DSCs prepared using spin cast films show good short-circuit current density (J_{SC}), which is comparable with that of WO_3 LB. This might be due to the fact that the work function (Φ) values for spin cast and LB films are close to the ionization potential of FTO ($\Phi_{FTO}\sim$5.1 eV) (Fig. S4, ESI†). Owing to the small difference, ohmic-like contact (Fig. S3a, ESI†)

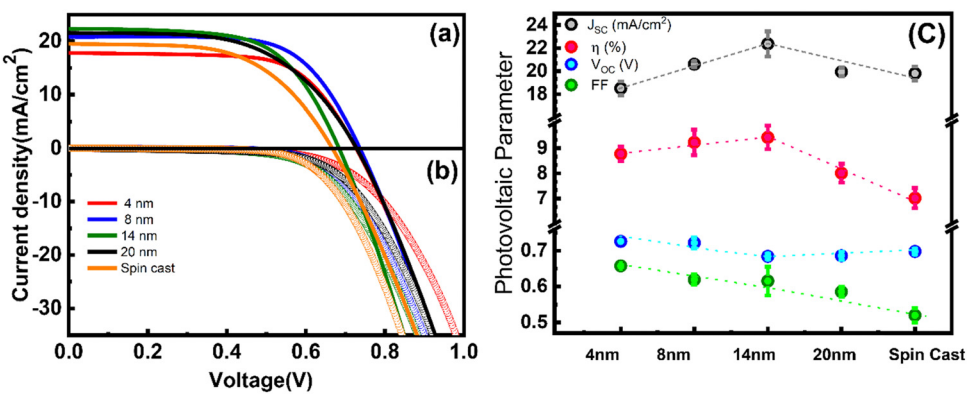

Fig. 6 (a) Typical photovoltaic (solid circles) and (b), dark characteristics (open circles) and (c) average values of estimated photovoltaic parameters of three DSCs, fabricated using BL of different thickness along with error values, under 1.5AM illumination (dashed lines are a guide for the eyes).

forms in both cases, resulting in comparable J_{SC}. Furthermore, there is a clear distinction in efficiency for DSCs fabricated with WO_3 BL thickness $\leq$14 nm and those with thickness $\sim$20 nm. The J_{SC}, FF and V_{OC} decrease with increase in the WO_3 blocking layer thickness to 20 nm, which is well above the L_D and is attributable to the bulk-effect.

Similar observations were reported for perovskite solar cells fabricated with ultra-thin films of NiO and SnO_2 as interfacial layers.[16,43] Seo *et al.* found that when the NiO film thicknesses decreased from 10–15 to 2.5–7.5 nm, the short-circuit current (J_{SC} $\sim$16.5 to $\sim$18.5 mA cm^{-2}) increased due to the improved conductivity of the film as the thickness is sufficient to be overlapped by L_D. In the case of the SnO_2 film, when the thickness is increased just above the L_D value, improvement in all photovoltaic parameters was observed due to enhanced charge extraction.[43] In both cases, the device efficiency decreased when the thicknesses of the buffer layer increased much higher than the Debye length. Since the thickness of the prepared WO_3 BL (4–14 nm) is less than the reported Debye length of WO_3, the improvement in the J_{SC} of the devices is due to nano effects. Beyond this thickness, the bulk property dominates and therefore, the J_{SC} decreases owing to the decrease in conductivity. Slightly reduced J_{SC} observed in DSCs fabricated with 4 nm WO_3 BL might be due to the limitation of FTO surface roughness, therefore resulting in slightly reduced efficiency. Nevertheless, improved V_{OC} and FF obtained for these devices are attributed to the fact that the thickness of BL is of the order of L_D. In this case, the WO_3 film is fully depleted, having minimal potential drop in the BL, as discussed in the earlier section for MS analysis. Improved charge transport and reduced recombination for DSCs employing thinner BLs ($\leq L_D$) as compared to that having thicker BL ($>L_D$) therefore gives rise to improved J_{SC} and FF and thereby enhanced efficiency. In all, high efficiency ($\sim$9.79%) observed for DSCs employing 14 nm thick WO_3 BL is the result of enhanced carrier density, conductivity, and the uniform and homogeneous surface, as well as excellent blocking behaviour as observed earlier. It is to be emphasized here that even a 4 nm thick WO_3 blocking layer is sufficient to serve the purpose of the blocking layer without compromising V_{OC} and FF.

To further investigate the influence of BL thickness on the device performance, we focus on dark current (Fig. 6(b)), which is generally dominated by the recombination through nanocrystalline TiO_2 particles or the exposure of the FTO substrate to the electrolyte. The onset potential for 4 nm thick WO_3 film is observed at voltage $>$0.56 V and shifts to lower potential 0.48 V for a WO_3 film thickness of 20 nm, in accordance with the *JV* data where a slight decrease in FF is observed for DSCs employing WO_3 BL. This result is consistent with earlier reports where thinner films have provided better charge extraction due to the space charge region effect.[43] In all, DSCs fabricated with BL of thickness $\leq$14 nm reveal better J_{SC}, FF, V_{OC} and efficiency as well as reduced dark current as compared to DSCs employed with BL of thickness $\sim$20 nm.

To substantiate the above findings, we investigated the devices further using impedance spectroscopy, under illumination as well as dark conditions (Fig. S5, ESI†). Various parameters, such as chemical capacitance (C_μ), recombination time, series resistance (R_s) and charge transfer resistance (R_{PT}) were estimated by fitting the Nyquist plots using the electrical circuit as described in Fig. S5(f) (ESI†)[3,4] and are presented in Fig. 7. The electrical circuit elements contributing to the photoanode impedance are dependent on the illumination as well as potential conditions as discussed below:

(i) EIS under 1 sun:

Under 1 sun illumination and at a potential equal to the open circuit potential, the chemical capacitance C_μ, represents the density of photogenerated electrons arising due to charge accumulation at the photoanode/electrolyte interface. The estimated R_s for DSCs comprises the bulk resistance of the photoanode, and contact resistance of all interfaces and the counter electrode as well as the connection resistance. Since all DSCs have the same layers except that the thickness of WO_3 BL is varied, any variation in R_s value may be attributable to the FTO/WO_3 and WO_3/m-TiO_2 interface. As shown in the figure, a slightly higher R_s is observed for DSCs having BL of thickness $\leq$9 nm than that for BL of thickness 14 nm, and this is attributable to the presence of fully depleted regions in thinner WO_3 BL as evident from MS results discussed earlier in Section 3.2. Furthermore, the recombination time and C_μ does not change much for DSCs fabricated with BL thickness $\leq$14 nm. However, a sudden drop is observed for DSCs based on 20 nm WO_3 BL. The high values of chemical capacitance and recombination suggest better charge transport and reduced recombination, leading to higher J_{SC}, V_{OC}

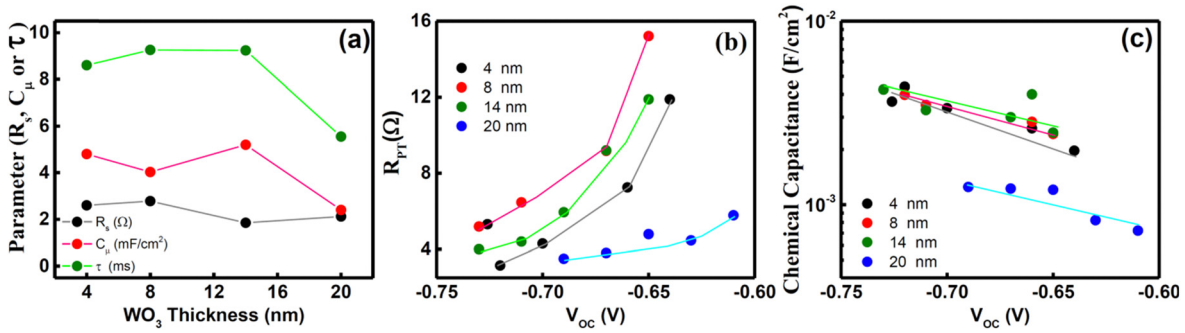

Fig. 7 (a) Extracted EIS parameters, R_S, C_μ and T from the EIS spectra recorded at V_{OC} of the respective device under AM 1.5 sun illumination and, estimated (b) charge transfer resistance and (c) chemical capacitance from dark EIS curves as a function of thickness of the WO_3 BL.

and FF for DSCs employing WO_3 BL of thickness $\leq$14 nm. This is consistent with our earlier observation on the CV and EIS results of WO_3, where a high carrier density and charge transfer resistance is associated with thinner WO_3 films (thickness $\leq$14 nm) and corroborates *JV* data.

(ii) Dark EIS:

Under dark conditions, the photoanode is insulating as no photoexcited electrons are injected into the conduction band of mesoporous TiO_2 and the value of recombination resistance is higher than that in 1 sun. This is due to the fact that the I_3^- is formed in proximity to the counter electrode and then it has to diffuse through the electrolyte before reaching the photoanode. The chemical capacitance ($C_{m\text{-}TiO_2}$) in this case arises mainly due to localized electron trapping states and therefore, accounts for the electron recombination at the m-TiO_2/electrolyte interface. Furthermore, the $C_{m\text{-}TiO_2}$ of the FTO/WO_3/m-TiO_2 photoanode in the dark shows an exponential rise with decrease in applied voltage. This is a behavior typical of the photoanode and is related to the total density of electrons in the dark, n, by the expression:[44]

$$C_{m\text{-}TiO_2} = \frac{ne^2}{kT} \quad (4)$$

where $n \propto n_{CB}^{\beta}$ and $1 > \beta > 0$ indicate an exponential distribution of traps below the conduction band edge.

The parameters deduced from dark EIS measurements, such as charge transfer resistance (R_{PT}) and $C_{m\text{-}TiO_2}$ of the m-TiO_2/electrolyte interface corroborate the EIS results under 1 sun. A clear distinction between DSCs employing BL having thickness $\leq$14 nm and 20 nm is observed in the R_{PT}–V_{OC} and $C_{m\text{-}TiO_2}$–V_{OC} curves, as shown in Fig. 7(b) and (c). The R_{PT} value increases exponentially with increase in the V_{OC}, and is consistent with earlier reports.[44] Higher R_{PT} values obtained for DSCs having WO_3 BL of thickness $\leq$14 nm, suggests reduced charge recombination at the m-TiO_2/electrolyte interface. A high value of $C_{m\text{-}TiO_2}$ observed in DSCs having BL of thickness $\leq$14 nm indicates reduced charge carrier density and therefore fewer defects as compared with that of DSCs with BL of thickness 20 nm.

The improved interfacial properties of the DSCs fabricated with BL of thickness $\leq$14 nm are further confirmed from IMVS and IMPS measurements (Fig. 8). IMPS and IMVS curves do not show much variation in shape when the thickness of the BL in DSC is varied from 4 nm to 14 nm. However, the DSCs fabricated with 20 nm and spin cast WO_3 film revealed development of an additional arc at lower frequency suggesting changes in the kinetics at the FTO/WO_3 interface. The appearance of an arc may be related to recombination due to the bulk-nature of the film.[45] The transport and recombination time for the device were calculated from the expression $T_n = 1/2\pi f_n$ and $T_R = 1/2\pi f_R$, respectively, where f_n (or f_R) is the characteristic frequency minimum of the imaginary component from the IMPS (or IMVS) data. The figure reveals that (i) the T_n and T_R

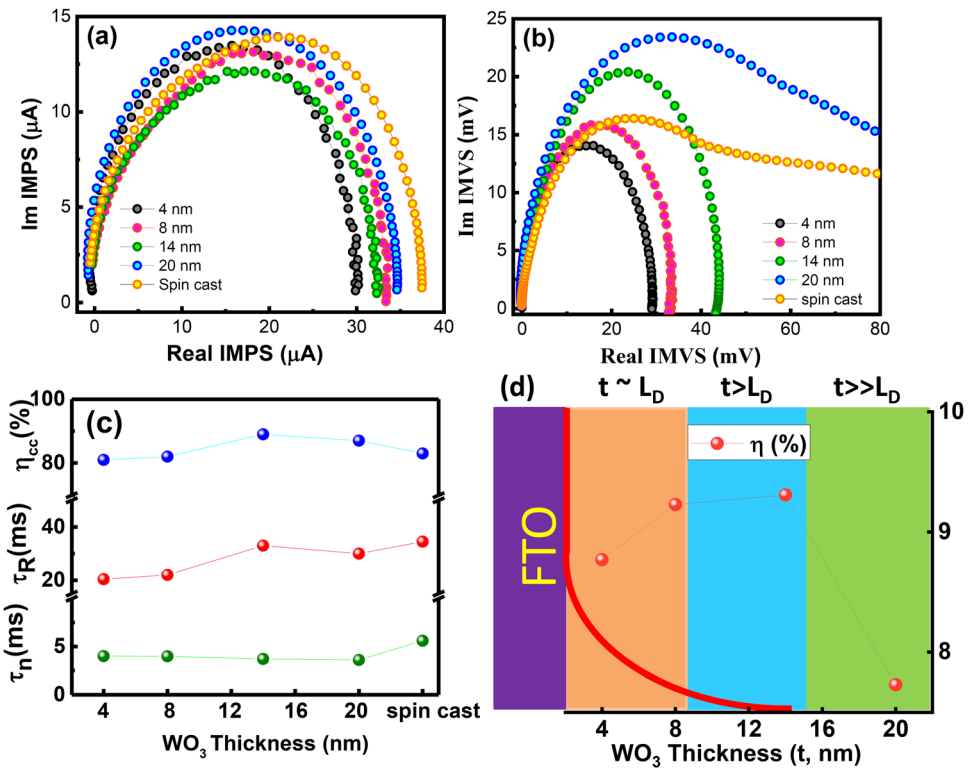

Fig. 8 (a) IMPS, (b) IMVS spectra and (c) estimated recombination time, transport time and collection efficiency as a function of WO_3 BL thickness; for comparison data for DSCs fabricated with spin cast WO_3 LB is also shown and (d) shows a schematic presentation of the influence of WO_3 BL thickness in the Debye length regime.

remain almost constant with thickness for DSCs fabricated with WO_3 BL $\leq$ 8 nm. (ii) A slight improvement in T_R and T_n is observed for DSC fabricated with BL $\geq$ 14 nm thick film and (iii) high T_n and low T_R values for DSCs employing spin cast films. These data are consistent with *JV* and EIS results of DSCs, which reveal higher J_{SC} and FF for DSCs based on WO_3 LB as compared with that of the spin cast film. Another important parameter of the DSCs, *viz*, electron collection efficiency can be estimated from the T_n and T_R values as follows:

$$\eta_{cc}(\%) = \left(1 - \frac{T_n}{T_R}\right) \times 100 \quad (5)$$

The η_{cc} of the DSCs based on 14 nm WO_3 BL is much higher than that of the 20 nm thick WO_3 BL and spin cast film and therefore, the best efficiency is obtained for the DSCs fabricated with 14 nm WO_3 BL. Since the only difference in fabricated DSCs is the BL, this suggests that in addition to providing faster transport and reduced recombination to the photogenerated electrons, the effect of WO_3 BL is manifested in the consecutive m-TiO_2 layers as well. The thin WO_3 BL ($\leq$14 nm) provides the ideal surface for the deposition of the m-TiO_2 for device fabrication and results in fewer defects. The above findings can be presented schematically in Fig. 8(d). As shown in the figure, the Debye length of WO_3 BL plays an important role in improving the device performance: DSCs fabricated with BL having thickness within L_D or near L_D perform much higher than the devices with thickness much higher than L_D.

4. Conclusion

In summary, we have successfully prepared ultra-thin compact BL (4–20 nm) in the range of Debye length by the LB method and studied the influence of BL thickness on DSC performance. A clear distinction in charge transport and blocking properties was observed between thin films ($\leq$14 nm) and thick films ($>$20 nm), which were related to L_D. Better interfacial properties as well as charge transport and blocking properties of DSC devices based on thin WO_3 blocking layers ($\leq$14 nm) result in higher efficiency up to $\sim$9.79% in DSCs devices as compared to DSCs having WO_3 BL of 20 nm thickness (8.02%) as well as those prepared with spin cast films (7%). This work demonstrates that employing WO_3 BL of the Debye length regime results in the enhancement of the efficiency of the solar cells without compromising optical transmittance and blocking properties.

Author contributions

N. Kumar: data curation, formal analysis. S. Choudhury: resources, validation. A. Mahajan: resources, validation. Vibha Saxena: conceptualization, data curation, formal analysis, project administration, resources, supervision, validation, visualization, writing – original draft writing – review & editing. All authors have read and agreed to the published version of the manuscript.

Data availability

The data supporting this article have been included as part of the ESI.†

Conflicts of interest

There are no conflicts of interest to declare.

Acknowledgements

The authors thank Dr S. M. Yusuf, Dr L. M. Pant and Dr A. Singh for the support of this work.

References

1 E. Pulli, E. Rozzi and F. Bella, Transparent photovoltaic technologies: current trends towards upscaling, *Energy Convers. Manage.*, 2020, **219**, 112982.
2 J.-M. Ji, H. Zhou, Y. K. Eom, C. H. Kim and H. K. Kim, 14.2% Efficiency Dye-Sensitized Solar Cells by Co-sensitizing Novel Thieno[3,2-*b*]indole-Based Organic Dyes with a Promising Porphyrin Sensitizer, *Adv. Energy Mater.*, 2020, **10**(15), 2000124.
3 P. Ledezma, J. Jermakka, J. Keller and S. Freguia, Impact of film thickness of ultra-thin dip-coated compact TiO_2 layers on the performance of mesoscopic perovskite solar cells, *Front. Microbiol.*, 2017, **8**, 750.
4 I. P. Liu, W.-H. Lin, C.-M. Tseng-Shan and Y.-L. Lee, Importance of Compact Blocking Layers to the Performance of Dye-Sensitized Solar Cells under Ambient Light Conditions, *ACS Appl. Mater. Interfaces*, 2018, **10**(45), 38900–38905.
5 W. Zhang, Y. Wu, H. W. Bahng, Y. Cao, C. Yi, Y. Saygili, J. Luo, Y. Liu, L. Kavan and J.-E. Moser, *et al.*, Comprehensive control of voltage loss enables 11.7% efficient solid-state dye-sensitized solar cells, *Energy Environ. Sci.*, 2018, **11**(7), 1779–1787, DOI: **10.1039/C8EE00661J**.
6 M.-E. Yeoh and K.-Y. Chan, Efficiency Enhancement in Dye-Sensitized Solar Cells with ZnO and TiO_2 Blocking Layers, *J. Electron. Mater.*, 2019, **48**(7), 4342–4350.
7 M. A. Arvizu, H.-Y. Qu, U. Cindemir, Z. Qiu, E. A. Rojas-González, D. Primetzhofer, C. G. Granqvist, L. Österlund and G. A. Niklasson, Electrochromic WO_3 thin films attain unprecedented durability by potentiostatic pretreatment, *J. Mater. Chem. A*, 2019, **7**(6), 2908–2918, DOI: **10.1039/C8TA09621J**.
8 L. You, B. Liu, T. Liu, B. Fan, Y. Cai, L. Guo and Y. Sun, Organic Solar Cells Based on $WO_{2.72}$ Nanowire Anode Buffer Layer with Enhanced Power Conversion Efficiency and Ambient Stability, *ACS Appl. Mater. Interfaces*, 2017, **9**(14), 12629–12636.
9 R. Shakoury, A. Arman, S. Rezaee, A. G. Korpi, S. Kulesza, C. Luna, M. Bramowicz and M. Mardani, Optical properties and morphology analysis of hexagonal WO_3 thin films obtained by electron beam evaporation, *J. Mater. Sci.: Mater. Electron.*, 2021, **32**(1), 798–805.

10 J. M. Berak and M. J. Sienko, Effect of oxygen-deficiency on electrical transport properties of tungsten trioxide crystals, *J. Solid State Chem.*, 1970, **2**(1), 109–133.
11 M. Miyakawa, K. Ueda and H. Hosono, Carrier generation in highly oriented WO_3 films by proton or helium implantation, *J. Appl. Phys.*, 2002, **92**(4), 2017–2022.
12 S. S. Patil, R. M. Mane, K. V. Khot, S. S. Mali, C. Kook Hong and P. N. Bhosale, Surfactant assisted approach to development of efficient WO_3 photoanode for natural dye sensitized solar cell, *Sol. Energy*, 2021, **220**, 371–383.
13 J. Zhang, C. Shi, J. Chen, Y. Wang and M. Li, Preparation of ultra-thin and high-quality WO_3 compact layers and comparision of WO_3 and TiO_2 compact layer thickness in planar perovskite solar cells, *J. Solid State Chem.*, 2016, **238**, 223–228.
14 D. Liu, Q. Wang, C. J. Traverse, C. Yang, M. Young, P. S. Kuttipillai, S. Y. Lunt, T. W. Hamann and R. R. Lunt, Impact of Ultrathin C60 on Perovskite Photovoltaic Devices, *ACS Nano*, 2018, **12**(1), 876–883.
15 M. T. Masood, C. Weinberger, J. Sarfraz, E. Rosqvist, S. Sandén, O. J. Sandberg, P. Vivo, G. Hashmi, P. D. Lund and R. Österbacka, *et al.*, Impact of Film Thickness of Ultrathin Dip-Coated Compact TiO_2 Layers on the Performance of Mesoscopic Perovskite Solar Cells, *ACS Appl. Mater. Interfaces*, 2017, **9**(21), 17906–17913.
16 S. Seo, I. J. Park, M. Kim, S. Lee, C. Bae, H. S. Jung, N.-G. Park, J. Y. Kim and H. Shin, An ultra-thin, un-doped NiO hole transporting layer of highly efficient (16.4%) organic–inorganic hybrid perovskite solar cells, *Nanoscale*, 2016, **8**(22), 11403–11412, DOI: 10.1039/C6NR01601D.
17 J. Kukkola, M. Mohl, A.-R. Leino, J. Mäklin, N. Halonen, A. Shchukarev, Z. Konya, H. Jantunen and K. Kordas, Room temperature hydrogen sensors based on metal decorated WO_3 nanowires, *Sens. Actuators, B*, 2013, **186**, 90–95.
18 H. Cheng, Y. Liu, B. Cai, C. Hägglund, T. Kubart, G. Boschloo and H. Tian, Atomic Layer Deposition of SnO_2 as an Electron Transport Material for Solid-State P-type Dye-Sensitized Solar Cells, *ACS Appl. Energy Mater.*, 2022, **5**(10), 12022–12028.
19 Y. Li, L. Ma, Y. Yoo, G. Wang, X. Zhang and M. J. Ko, Atomic layer deposition: A versatile method to enhance TiO_2 nanoparticles interconnection of dye-sensitized solar cell at low temperature, *J. Ind. Eng. Chem.*, 2019, **73**, 351–356.
20 S. Seo, S. Jeong, H. Park, H. Shin and N.-G. Park, Atomic layer deposition for efficient and stable perovskite solar cells, *Chem. Commun.*, 2019, **55**(17), 2403–2416, DOI: 10.1039/C8CC09578G.
21 Y. Kuang, V. Zardetto, R. van Gils, S. Karwal, D. Koushik, M. A. Verheijen, L. E. Black, C. Weijtens, S. Veenstra and R. Andriessen, *et al.*, Low-Temperature Plasma-Assisted Atomic-Layer-Deposited SnO_2 as an Electron Transport Layer in Planar Perovskite Solar Cells, *ACS Appl. Mater. Interfaces*, 2018, **10**(36), 30367–30378.
22 S. Balasubramanyam, A. Sharma, V. Vandalon, H. C. M. Knoops, W. M. M. Kessels and A. A. Bol, Plasma-enhanced atomic layer deposition of tungsten oxide thin films using $(t\mathrm{BuN})_2(\mathrm{Me_2N})_2\mathrm{W}$ and O_2 plasma, *J. Vac. Sci. Technol., A*, 2018, **36**(1), 01B103.
23 A. Jelinska, K. Bienkowski, M. Jadwiszczak, M. Pisarek, M. Strawski, D. Kurzydlowski, R. Solarska and J. Augustynski, Enhanced Photocatalytic Water Splitting on Very Thin WO_3 Films Activated by High-Temperature Annealing, *ACS Catal.*, 2018, **8**(11), 10573–10580.
24 N. A. Isaac, M. Valenti, A. Schmidt-Ott and G. Biskos, Characterization of Tungsten Oxide Thin Films Produced by Spark Ablation for NO_2 Gas Sensing, *ACS Appl. Mater. Interfaces*, 2016, **8**(6), 3933–3939.
25 G. Mattoni, A. Filippetti, N. Manca, P. Zubko and A. D. Caviglia, Charge doping and large lattice expansion in oxygen-deficient heteroepitaxial WO_3, *Phys. Rev. Mater.*, 2018, **2**(5), 053402.
26 G. Mattoni, B. de Jong, N. Manca, M. Tomellini and A. D. Caviglia, Single-Crystal Pt-Decorated WO_3 Ultrathin Films: A Platform for Sub-ppm Hydrogen Sensing at Room Temperature, *ACS Appl. Nano Mater.*, 2018, **1**(7), 3446–3452.
27 M. A. Mamun, K. Zhang, H. Baumgart and A. A. Elmustafa, Nanomechanical and Morphological Characterization of Tungsten Trioxide (WO_3) Thin Films Grown by Atomic Layer Deposition, *ECS J. Solid State Sci. Technol.*, 2015, **4**(9), P398.
28 S. Balasubramanyam, A. Sharma, V. Vandalon, H. C. M. Knoops, W. M. M. Kessels and A. A. Bol, Plasma-enhanced atomic layer deposition of tungsten oxide thin films using $(t\mathrm{BuN})_2(\mathrm{Me_2N})_2\mathrm{W}$ and O_2 plasma, *J. Vac. Sci. Technol., A*, 2017, **36**(1), 01B103.
29 O. Prakash, V. Saxena, R. K. Bedi, A. K. Debnath and A. Mahajan, Solution processable transition metal oxide ultra-thin films as alternative electron transport and hole blocking layers in dye sensitized solar cells, *J. Photochem. Photobiol., A*, 2021, **418**, 113385.
30 V. Saxena, N. Bhagat, S. Choudhury, A. Mahajan and A. Singh, Phase Variation of Ultrathin WO_3 Electron-Transport Layer Prepared by Scalable Langmuir–Blodgett Technique to Boost Efficiency of Dye Sensitized Solar Cells, *Solar RRL*, 2022, **6**(8), 2200222.
31 Z. Avazbaeva, W. Sung, J. Lee, M. D. Phan, K. Shin, D. Vaknin and D. Kim, Origin of the Instability of Octadecylamine Langmuir Monolayer at Low pH, *Langmuir*, 2015, **31**(51), 13753–13758.
32 J. T. Davies, E. K. Rideal and S. A. Rice, Interfacial Phenomena, *Phys. Today*, 1962, **15**(4), 78.
33 J. Li, Y. Liu, Z. Zhu, G. Zhang, T. Zou, Z. Zou, S. Zhang, D. Zeng and C. Xie, A full-sunlight-driven photocatalyst with super long-persistent energy storage ability, *Sci. Rep.*, 2013, **3**(1), 2409.
34 O. Prakash, V. Saxena, S. Choudhury, Tanvi, A. Singh, A. K. Debnath, A. Mahajan, K. P. Muthe and D. K. Aswal, Low temperature processable ultra-thin WO_3 Langmuir-Blodgett film as excellent hole blocking layer for enhanced performance in dye sensitized solar cell, *Electrochim. Acta*, 2019, **318**, 405–412.
35 C. V. Ramana, S. Utsunomiya, R. C. Ewing, C. M. Julien and U. Becker, Structural Stability and Phase Transitions in WO_3 Thin Films, *J. Phys. Chem. B*, 2006, **110**(21), 10430–10435.
36 Tanvi, V. Saxena, A. Singh, O. Prakash, A. Mahajan, A. K. Debnath, K. P. Muthe and S. C. Gadkari, Improved

performance of dye sensitized solar cell via fine tuning of ultra-thin compact TiO_2 layer, *Sol. Energy Mater., Sol. Cells*, 2017, **170**, 127–136.

37 R. Memming, *Semiconductor Electrochemistry*, Wiley, 2015.

38 Y. Matsumoto, Y. Miura and S. Takata, Thickness-Dependent Flat Band Potential of Anatase TiO_2(001) Epitaxial Films on Nb:$SrTiO_3$(001) Investigated by UHV-Electrochemistry Approach, *J. Phys. Chem. C*, 2016, **120**(3), 1472–1477.

39 P. Xu, T. J. Milstein and T. E. Mallouk, Flat-Band Potentials of Molecularly Thin Metal Oxide Nanosheets, *ACS Appl. Mater. Interfaces*, 2016, **8**(18), 11539–11547.

40 A. Sacco, Electrochemical impedance spectroscopy: fundamentals and application in dye-sensitized solar cells, *Renewable Sustainable Energy Rev.*, 2017, **79**, 814–829.

41 L. Kavan, N. Tétreault, T. Moehl and M. Grätzel, Electrochemical Characterization of TiO_2 Blocking Layers for Dye-Sensitized Solar Cells, *J. Phys. Chem. C*, 2014, **118**(30), 16408–16418.

42 J. Premkumar, Development of Super-Hydrophilicity on Nitrogen-Doped TiO_2 Thin Film Surface by Photoelectrochemical Method under Visible Light, *Chem. Mater.*, 2004, **16**(21), 3980–3981.

43 S. S.-O. Youn, J. Kim, J. Na, W. Jo and G. Y. Kim, Understanding the Space-Charge Layer in SnO_2 for Enhanced Electron Extraction in Hybrid Perovskite Solar Cells, *ACS Appl. Mater. Interfaces*, 2022, **14**(42), 48229–48239.

44 F. Fabregat-Santiago, J. Bisquert, G. Garcia-Belmonte, G. Boschloo and A. Hagfeldt, Influence of electrolyte in transport and recombination in dye-sensitized solar cells studied by impedance spectroscopy, *Sol. Energy Mater. Sol. Cells*, 2005, **87**(1), 117–131.

45 A. Pockett, M. Spence, S. K. Thomas, D. Raptis, T. Watson and M. J. Carnie, Beyond the First Quadrant: Origin of the High Frequency Intensity-Modulated Photocurrent/Photovoltage Spectroscopy Response of Perovskite Solar Cells, *Solar RRL*, 2021, **5**(5), 2100159.